PCCP

RSC Publishing

PAPER

View Article Online
View Journal | View Issue

Cite this: *Phys. Chem. Chem. Phys.*, 2013, **15**, 4625

Density functional theory study on the adsorption and decomposition of the formic acid catalyzed by highly active mushroom-like Au@Pd@Pt tri-metallic nanoparticles†

Sai Duan,[ab] Yong-Fei Ji,[b] Ping-Ping Fang,[a] Yan-Xia Chen,[c] Xin Xu,[d] Yi Luo*[bc] and Zhong-Qun Tian*[a]

Received 14th November 2012,
Accepted 28th January 2013

DOI: 10.1039/c3cp44053b

www.rsc.org/pccp

Local structures and adsorption energies of a formic acid molecule and its decomposed intermediates (H, O, OH, CO, HCOO, and COOH) on highly electrocatalytically active mushroom-like Au-core@Pd-shell@Pt-cluster nanoparticles with two atomic layers of the Pd shell and stoichiometric Pt coverage of around half-monolayer (Au@2 ML Pd@0.5 ML Pt) have been investigated by first principles calculations. The adsorption sites at the center (far away from the Pt cluster) and the edge (close to the Pt cluster) are considered and compared. Significant repulsive interaction between the edge sites and CO is observed. The calculated potential energy surfaces demonstrate that, with respect to the center sites, the CO_2 pathway is considerably promoted in the edge area. Our results reveal that the unique edge structure of the Pt cluster is responsible for the experimentally observed high electrocatalytic activity of the Au@Pd@Pt nanoparticles toward formic acid oxidation. Such microscopic understanding should be useful for the design of new electrochemical catalysts.

1 Introduction

Metal nanoparticles (NPs) with high electrocatalytic activities have become important elements in electrochemistry, especially in electrocatalysis, over the last two decades. The most attractive feature of the NPs is their tunability that allows the catalytic activity to be enhanced by altering the shape of the NPs,[1–4] modifying the adsorbate[5,6] and changing the surface compositions and morphologies.[7–9] The latter is particularly exciting since it has extended the applicability of the NPs from the mono-metallic to bi-metallic and even tri-metallic systems.[9–13]

Formic acid (HCOOH) can provide higher power density than many other fuels in the direct fuel cells.[14] It is nontoxic and exhibits small crossover flux through Nafion,[15] allowing us to use high concentration of fuel.[16] All these properties have made direct formic acid fuel cells (DFAFCs) a good candidate for portable device applications.[17,18] Platinum (Pt) surfaces have shown remarkable intrinsic activity for the oxidation of formic acid.[19] However, it is well known that Pt catalysts are often poisoned by the decomposed intermediate carbon monoxide (CO).[20] This is often referred to as the indirect pathway of the oxidation of formic acid. On the other hand, palladium (Pd) based catalysts have been reported as a way to circumvent this problem, on which the formic acid is oxidized *via* a more direct pathway, *i.e.* producing carbon dioxide (CO_2) directly without going through the strongly adsorbed CO intermediate.[21–24] Previous studies showed that the apparent activity (averaged over all the catalysts surface) of Pd NPs for formic acid is higher than that of Pt NPs.[9,25,26] It is thus worth combining the benefits of Pd and Pt to design the catalysts for DFAFCs. As a result, Pt–Pd bi-metallic NPs have been widely investigated in DFAFCs.[8,27–30]

Due to the limited natural resources, it is highly desirable to use catalysts with less rare metals or completely earth-abundant materials.[31–33] Recently, our group rationally synthesized tri-metallic NPs by the seed-mediated growth method,

[a] *State Key Laboratory of Physical Chemistry of Solid Surfaces and College of Chemistry and Chemical Engineering, Xiamen University, Xiamen 361005, P. R. China. E-mail: zqtian@xmu.edu.cn; Fax: +86 (0)592 2085349; Tel: +86 (0)592 2182536*

[b] *Department of Theoretical Chemistry and Biology, School of Biotechnology, Royal Institute of Technology, S-106 91 Stockholm, Sweden. E-mail: luo@kth.se; Fax: +46 (0)8 55378414; Tel: +46 (0)8 55378590*

[c] *Hefei National Laboratory for Physical Sciences at the Microscale, University of Science and Technology of China, Hefei, Anhui 230026, P. R. China*

[d] *MOE Laboratory for Computational Physical Sciences, Department of Chemistry, Fudan University, Shanghai 200433, P. R. China*

† Electronic supplementary information (ESI) available: Optimized structures of further decomposed species or the species adsorbed on the Pt clusters as well as all OH adsorption configurations in the center area. See DOI: 10.1039/c3cp44053b

which consists of a gold (Au) core covered by a Pd shell with deposited Pt clusters, *i.e.* a Au@Pd@Pt system.[9] We have made different compounds by systematically changing the thickness of the Pd shell and the loading of the Pt clusters, and found that Au@Pd@Pt NPs with two layers of the Pd shell and a half monolayer of stoichiometric Pt clusters (denoted Au@2 ML Pd@0.5 ML Pt NPs hereafter) display the highest electrocatalytic activity toward HCOOH oxidation.[9] It was demonstrated that at 0.0 V with respect to a saturated calomel electrode (SCE), the activity for HCOOH oxidation–reduction of Au@2 ML Pd@0.5 ML Pt NPs is ~5 times higher than that of the pure Pd surface and ~100 times higher than that of the pure Pt surface under steady state conditions.[9] The surface-enhanced Raman spectra (SERS) of CO adsorbed on Au@Pd@Pt NPs in a CO-saturated solution have been used to determine the local structure of the Pt cluster. One important experimental observation was that the frequency of CO adsorbed on the Pd surface red-shifted by ~25 cm^{-1} when the stoichiometric Pt coverage increased from 0 to 1 monolayer.[9,34] We carried out systematically density functional theory (DFT) calculations to simulate Raman spectra of CO for a large number of possible adsorption configurations and reproduced the experimentally observed Pt coverage dependent spectra when the Pt cluster adopts a unique mushroom-like structure, rather than the island-like structure following the Volmer–Weber growth model.[34]

In the present study, we continue our study using DFT calculations to determine the local structures of the formic acid molecule, the decomposed intermediates from HCOOH and the oxidants, as well as their adsorption energies at Au@2 ML Pd@0.5 ML Pt NPs. Moreover, the direct and indirect pathways of COOH oxidation are also investigated. We found that the high electrocatalytic activity of Au@Pd@Pt NPs is originated from the synergistic interaction of Pd and Pt at the edge sites of the mushroom-like structures.

2 Computational details

All calculations were performed using Vienna *ab initio* simulation package (VASP).[35] The Perdew–Burke–Ernzerhof generalized-gradient approximation (GGA-PBE)[36] exchange–correlation functional with the projector augmented-wave method (PAW),[37,38] which was generated by taking scalar relativistic corrections into account, was employed. The energy cut off of the plane-wave basis set for the wave functions was set to 400 eV. The Gaussian smearing method with a broadening factor of 0.01 eV for gas phase calculations was used to improve convergence while the Methfessel and Paxton method with a broadening factor of 0.1 eV was adopted for the condensed phase.[39] All total energies were extrapolated to 0 K while no artificial entropy was included in the calculated energies of species in gas phase. Since the entropy contributions to the free energy in heterogeneous catalytic reactions are usually quite small[40] and the difference of entropy as well as zero point energy contribution between the reactant and the product will be even smaller, the 0 K energies used here are thus reasonable.

We have considered the following reactions of HCOOH decomposition in DFAFCs[41]

$$HCOOH \rightarrow HCOO + H \quad (a)$$

$$HCOO \rightarrow CO_2 + H \quad (b)$$

$$CO_2 \rightarrow CO + O \quad (c)$$

$$HCOOH \rightarrow COOH + H \quad (d)$$

$$COOH \rightarrow CO + OH \quad (e)$$

$$COOH \rightarrow CO_2 + H \quad (f)$$

$$OH \rightarrow O + H \quad (g)$$

which lead to 9 species, *i.e.* H, O, OH, CO, HCOO, $COOH_u$, $COOH_d$, $HCOOH_u$, and $HCOOH_d$, respectively, adsorbed on the metal surface. Here the subscripts "u" and "d" represent the relative "up" and "down" positions of the hydrogen atom toward the metal surface (see Fig. 1 for details). In the gas phase, they were put in a large cubic box with a length of 30 Å to avoid lateral interactions. The symmetry was turned off by choosing the size of the supercell as 30.1 × 30.0 × 30.2 Å to avoid the artificial entropy. Spin-polarized DFT calculations were performed when necessary, *i.e.* for H, O at the triplet state, O_2, HCOO, COOH and OH, respectively. Full geometrical optimizations have been done with the final forces less than 0.02 eV $Å^{-1}$. Only a Gamma point was considered for the *k*-point sampling.

For the calculations of the condensed phase, the optimized lattice constant for Au is found to be 4.174 Å, which is in good agreement with the experimental value of 4.078 Å.[42] We used the same model system[34] to simulate the substrate, *i.e.* Au@2 ML Pd@0.5 ML Pt NPs, which exhibited the highest electrocatalytic activity.[9] This model system consists of two Au slab layers on the bottom and two Pd slab layers on the top, since the Pd atoms can be epitaxially deposited on the Au core. As a result, the Pd layers had the same lattice constant as the Au core in our calculations.[34] In the area where a $c(4 \times 2)$ unit cell is expanded to 3 × 3, a mushroom-like Pt_{17} cluster composed of 5 layers with the number of Pt atoms being 3, 3, 7, 3, and 1 in each layer

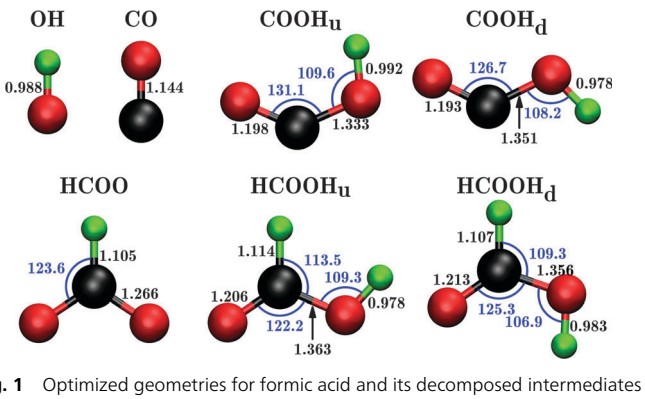

Fig. 1 Optimized geometries for formic acid and its decomposed intermediates (except for H and O atoms) in gas phase. Black, red, and green balls represent carbon, oxygen, and hydrogen atoms, respectively. Meanwhile, bond length in Å and angels in degrees are labeled as black and blue numbers, respectively.

from the bottom to top, respectively, was deposited on it.[34] The stoichiometric Pt coverage of this model is 47% which is close to the Pt loading of Au@2 ML Pd@0.5 ML Pt NPs with the highest electrocatalytic activity observed in experiments, *i.e.* 50%.[9] We should emphasize that this theoretical model could be a simplified mushroom-like structure of Au@2 ML Pd@0.5 ML Pt NPs. However, it has the capacity to reproduce the experimental SERS spectra as demonstrated in our previous studies.[34] It is reasonable to expect that this model contains the key structural characters of Au@2 ML Pd@0.5 ML Pt NPs. It is noted that the surface curvature of NPs was neglected in present simulations since the diameter of NPs is as large as 55 nm.[9] All positions of Au atoms were fixed to mimic the Au core, while, other atoms of the substrate were only optimized along the *z*-axis, which is the normal to the surface. Whereas, all atoms of adsorbates including anchoring atoms were optimized in all directions. For the atoms, *i.e.* H and O, adsorbed on the Au@2 ML Pd@0.5 ML Pt NPs, the anchoring atoms were obviously themselves. The anchoring atoms were O and C for OH and CO, respectively, while C for both $COOH_u$ and $COOH_d$. On the other hand, the anchoring atoms of HCOO, $HCOOH_u$ and $HCOOH_d$ were C when they were adsorbed on bridge, face-centered cubic (fcc), and hexagonal close-packed (hcp) sites. Meanwhile, when HCOO, $HCOOH_u$ and $HCOOH_d$ were adsorbed on top sites, the anchoring atoms were the O which were not bonded with H. Since we used a large super-cell that contains 161 metal atoms to simulate the substrate in the calculations, only the Gamma point was used for the *k*-point sampling and the final forces were also less than 0.02 eV $Å^{-1}$. Our test calculations show that, compared to the Gamma only sampling, the adsorption energy of CO on the fcc site in the center area decreases only by 0.05 eV with the extensive *k*-point sampling, *i.e.* a $3 \times 3 \times 1$ mesh grid. This result manifests that the Gamma only approach is suitable for current calculations. We also took the dipole correction along the *z*-axis into account during the calculations.[43,44]

The adsorption energy is defined as

$$E_{ad} = E_{Sub} + E_{Mol} - E_{tot} \quad (1)$$

where E_{Sub}, E_{Mol}, and E_{tot} represent the total energies of the model system for the substrate, the adsorbed species in vacuum, and the adsorbed system, respectively. Conveniently, here the E_{Mol} for H and O adsorbates was chosen as $\frac{1}{2}E_{H_2}$ and $\frac{1}{2}E_{O_2}$ respectively.

The transition states in the edge area were found by the nudged elastic band method with the image climbing (CNEB) method[45,46] with the force convergence criterion of 0.05 eV $Å^{-1}$. We found that it is difficult to locate the transition states in the center area by the CNEB method. Therefore, the CNEB[45,46] combined with the dimer method[47] was used for searching the transition states in the center area with the same threshold.

3 Results and discussion

3.1 Gas phase

Since the energy of the adsorbed species is the basic parameter for the adsorption energy calculation, we first investigate all substances in gas phase. The optimized geometries of OH, CO, HCOO, $COOH_u$, $COOH_d$, $HCOOH_u$, and $HCOOH_d$ are depicted in Fig. 1, which are generally in very good agreement with experimental measurements.[48–51] Nevertheless, the calculated bond lengths of OH and CO are 0.018 and 0.016 Å larger than the corresponding experimental values, respectively.[48,49] The calculated structure parameters for formic acid are listed in Table 1. For $HCOOH_d$, the largest deviation is only 0.005 Å for the bond length, and around 2° for the bond angle in comparison with the experimental results in vacuum.[50] For $HCOOH_u$, the largest deviation for the bond length is slightly larger, about 0.022 Å, while for the angle it is around 1.2°.[51] In general, our calculated structures for all species are in good agreement with previous theoretical results.[52–54] For example, the structure difference between results of the current GGA functional (PBE) and the previous hybrid functional (B3LYP) for HCOO is around 0.01 Å and 0.1° for bond lengths and angles respectively.[52]

Table 1 Comparison of the calculated and experimental geometries (bond lengths *r* in Å and angles δ in degrees) of formic acid in gas phase

	$HCOOH_d$		$HCOOH_u$	
	Calculated	Expt.[a]	Calculated	Expt.[b]
r_{C-H}	1.107	1.106	1.114	1.105
r_{C-O}	1.213	1.217	1.206	1.195
r_{C-OH}	1.356	1.361	1.363	1.352
r_{O-H}	0.983	0.984	0.978	0.956
δ_{H-C-OH}	109.3	109.1	113.5	114.6
δ_{C-O-H}	106.9	107.3	109.3	109.7
δ_{O-C-OH}	125.3	123.4	122.2	122.1

[a] Ref. 50. [b] Ref. 51.

It is worth mentioning that with the functional used, not only the optimized geometries but also the calculated relative energies are reliable. It is noted that the calculated energy separation between ^1D and ^3P states in the oxygen atom is 1.89 eV, in good agreement with the experimental value of 1.97 eV.[55] The calculated isomerization energy between $HCOOH_d$ and $HCOOH_u$ is 0.17 eV, which is in the range of previous theoretical prediction, 0.16 to 0.20 eV, from different methods.[53,54,56,57] Meanwhile, we have also found that the isomerization energy between $COOH_d$ and $COOH_u$ is 0.08 eV. Our calculated bond energy of O–H in formic acid is 4.73 eV, which also fits well with the experimental measurement, 4.66 eV.[58] Moreover, the predicted C–H bond energy in formic acid is found to be 0.4 eV lower than that of the O–H bond, consistent with the experimental observation.[58]

3.2 Adsorption of H, O, OH, and CO

We first discuss how the simpler species, *i.e.* H, O, OH, and CO, are adsorbed on the Au@2 ML Pd@0.5 ML Pt NPs. In this study, we have limited the calculations to two areas on the epitaxially deposited Pd surfaces of Au@2 ML Pd@0.5 ML Pt NPs. One of them is far from the mushroom-like Pt cluster labeled as "center" area, while the other is near the Pt cluster labeled as "edge" area. In each area, four typical adsorption sites, namely the bridge, fcc, hcp, and top sites, are considered.

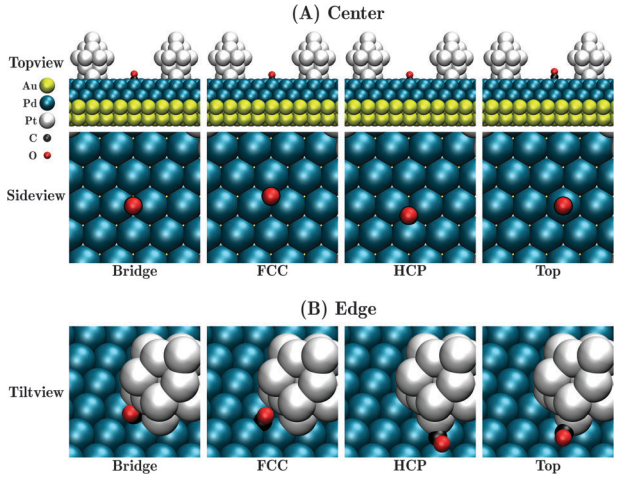

Fig. 2 Schematic adsorption areas (A) center and (B) edge as well as adsorption sites, *i.e.* bridge, fcc, hcp, and top from left to right, with optimized structures of CO adsorbed on Au@2 ML Pd@0.5 ML Pt NPs.

These adsorption sites in both areas are illustrated in Fig. 2 with the optimized CO/NPs structures as examples. In the center area the direct interaction between the adsorbed species and Pt clusters can be neglected because of the large distance between them. On the other hand, the adsorbed species in the edge area are significantly influenced by the Pt cluster simply due to the geometrical reason.

All the calculated adsorption energies using eqn (1) are listed in Table 2. It shows that H and O atoms prefer to adsorb on the three-fold sites, *i.e.* the fcc and hcp sites, in the center area of Au@2 ML Pd@0.5 ML Pt NPs. Moreover, H adsorbed on the bridge site as well as O adsorbed on the bridge and the top sites are unstable. The optimized geometries show that, finally, these unstable adsorbates can be stabilized when they adsorbed on the fcc site during optimizations. For H, the fcc and hcp sites are almost degenerate and more favorable than the top site. Whereas, for the adsorbed O, the fcc site is the local minimum. These results are consistent with previous theoretical findings for H and O atoms adsorbed on the pure Pd(111) surface.[59,60]

In the edge area, the situation becomes different. For the H atom, the top site is more stable (~0.5 eV lower in energy) compared with that in the center area. As a result, the top site and three-fold sites are almost degenerate and their adsorption energies are lower by ~0.1 eV than that on the hollow sites in the center area. When the O atom is adsorbed in the edge area, the adsorption energy on both the fcc and hcp sites is ~1.0 eV. Moreover, the O and H atoms adsorbed on the bridge site will change to the stable adsorption on the fcc site, meanwhile, the optimized structure of O adsorbed on the top site shows that O atoms are directly adsorbed on the Pt cluster (see Fig. S1 in ESI† for details).

The OH radical is aligned when adsorbed on hollow sites in the center area, and tilted on the bridge sites. We also found that the OH adsorbed on the top site is not stable and finally transferred to the bridge site with a tilted configuration (see Fig. S2 in ESI† for details). The most stable site for the adsorbed OH in the center area is the fcc site. Meanwhile, the tilted adsorption on the bridge site gives almost degenerate adsorption energy compared with that on the fcc site. The adsorption energy on the hcp site is lower than that on bridge and fcc sites and decreases successively. This tendency coincides with the previous DFT calculations for the OH adsorbed on pure Pd(111) surfaces.[61] The adsorption energy on the fcc site in the edge area is 0.38 eV unfavorable than that in the center area for the adsorbed OH on Au@2 ML Pd@0.5 ML Pt NPs, while the unfavorable value for the hcp is found to be 0.88 eV. For the top site, the optimized structure shows that the OH is adsorbed on the Pt clusters rather than on the Pd surface (see Fig. S2 in ESI† for details).

The CO molecule is vertically adsorbed on all sites in the center area as well as on the fcc site in the edge area (see Fig. 2). The fcc and hcp sites are degenerate for CO adsorbed in the center area while the top site is the most unfavorable site, which can also be found from the previous experimental and theoretical studies for CO adsorbed on pure Pd(111) surfaces.[62–65] The stabilization of CO adsorption at the three-fold sites is also supported by our previous *in situ* SERS experiments at relatively low surface coverage.[9] Calculated results show that the repulsion between CO and edge sites is significant. Specifically, the adsorption energy of the CO on the fcc, hcp and bridge sites in the edge area is 0.44, 0.58 and 0.94 eV smaller than those in the center area, respectively. Whereas, the value on the top site is increased by 0.39 eV. As a result, the top site in the edge area is the most stable one for CO adsorption. This result indicates that adsorption of the poison intermediate of the DFAFCs process, *i.e.* CO, is unfavorable in the edge area around the fcc site (see Fig. 2) of Au@Pd@Pt NPs. We have found that the dipole moments of the whole system are 0.26 and 0.11 Debye nm^{-2} for CO adsorbed in the edge and center areas, respectively. This indicates that the charge transfer between CO and Au@Pd@Pt NPs is quite different. The unstable CO in the edge area should thus be attributed to the

Table 2 Adsorption energy in eV of formic acid and its decomposition species at bridge (B), fcc (F), hcp (H), and top (T) sites on center and edge areas of Au@2 ML Pd@0.5 ML Pt surfaces. The reference states for H and O are $\frac{1}{2}E_{H_2}$ and $\frac{1}{2}E_{O_2}$ respectively

	Center				Edge[a]			
Species	B	F	H	T	B	F	H	T
H	—[b]	0.80	0.77	0.14	—[b]	0.70	0.62	0.63
O	—[b]	1.43	1.23	—[b]	—[b]	0.95	0.96	—[c]
OH	2.39	2.43	2.19	—[d]	—[b]	2.05	1.31	—[c]
CO	1.81	2.04	2.03	1.31	0.87	1.60	1.45	1.70
HCOO	2.36	—[d]	—[d]	1.63		2.35		
$HCOOH_u$	−0.05	—[d]	—[d]	−0.03		0.14		
$HCOOH_d$	0.16	0.17	0.18	−0.07		0.18		
$COOH_u$	2.13	2.14	2.12	1.91		1.88		
$COOH_d$	2.09	2.15	2.11	—[e]		1.95		

[a] HCOO, HCOOH, and COOH are as close as possible to the Pt cluster. [b] Adsorbed on the fcc site after optimization. [c] Adsorbed on Pt clusters after optimization. [d] Adsorbed on the bridge site after optimization. [e] Optimized structure essentially as that on the bridge site.

synergistic geometrical and electronic effects. Hence, it can be expected that the existence of the poison CO will be significantly hindered in some edge areas, although CO molecules may be generated during the DFAFCs process. Note that the edge area contains the Pd and Pt compositions. Thus, the CO unpoisoned edge area can keep the Pt in this area always "clean". Since the intrinsic activity of Pt is high,[19] the "clean" Pt may well explain the high electrocatalytic activity of the NPs for DFAFCs.

3.3 Adsorption of HCOO, COOH, and HCOOH

In this section, we discuss how the more complex species, *i.e.* HCOO, $COOH_u$, $COOH_d$, $HCOOH_u$, and $HCOOH_d$, are adsorbed on the Au@2 ML Pd@0.5 ML Pt NPs. All optimized structures adsorbed in the center area are depicted in Fig. 3. The optimized geometry shows that HCOO is normally adsorbed on the bridge site without rotation from its initial structure in the *x*–*y* plane. The bridge site is the most favorable site as displayed in Table 2 and the optimized configurations on the hollow sites are the same as those on the bridge site. The top site adsorption is vertical, which is 0.73 eV unfavorable than the bridge site adsorption. The prediction of HCOO adsorbed on the bridge site in the center area of Au@2 ML Pd@0.5 ML Pt NPs agrees well with previous experimental study of a formate anion adsorbed on the pure Pd(111) surface.[66,67] The adsorbed structure of $HCOOH_u$ in the center area is similar to HCOO as shown in Fig. 3. Only stable configurations exist on the bridge and top sites, while the optimized structures on the hollow site are essentially the same as those on the bridge site. The calculated results demonstrate that the interaction between $HCOOH_u$ and the Pd surface is very weak. The bridge site even shows stronger repulsion for the adsorption of HCOOH (see Table 2 for details). The most favorable adsorption site for $HCOOH_u$ is the top site where the adsorption energy is less than 0.1 eV, consistent with the previous theoretical result for the HCOOH adsorbed on the pure Pd(100) surface.[41] Whereas the interaction between $HCOOH_d$ and the Pd surface is attractive except the adsorption on the top site. The bridge, fcc, and hcp sites are degenerate for $HCOOH_d$ adsorption, meanwhile, the top site is the most unfavorable one. These results can be attributed to the attraction between the downward hydrogen in $HCOOH_d$ and the Pd surface.

The optimized structure of $COOH_u$ adsorbed on the bridge site shows a 90° rotation from the initial structure in the *x*–*y* plane while there is no rotation for the $COOH_d$ adsorption (see Fig. 3 for details). Meanwhile, the calculated adsorption energies show that the fcc site is the most favorable site for both adsorbates (see Table 2 for details). When adsorbed on the hollow sites, a rotation of 30° from the initial structures in the *x*–*y* plane is observed (see Fig. 3 for details). All adsorption energies of COOH on the bridge and hollow sites are around 2.10 eV in the center area. $COOH_u$ employs an unperturbed configuration on the top site with adsorption energies around 1.9 eV, meanwhile, $COOH_d$ has essentially the same configuration as that on the bridge site (see Fig. 3 for details).

When these species are adsorbed on the edge area, the Pt cluster has obviously a larger influence on them because of their larger sizes compared to the simpler adsorbates. As a result, we only considered the adsorbates adsorbed as close as possible to the Pt cluster. The optimized structures are shown in Fig. 4. Compared to the center area, the adsorption energies are almost the same for HCOO and $HCOOH_d$. Whereas, for COOH, the adsorption energies are slightly lower than those in the center area. On the other hand, the adsorption energy of $HCOOH_u$ in the edge area is even higher by ~0.2 eV than that in

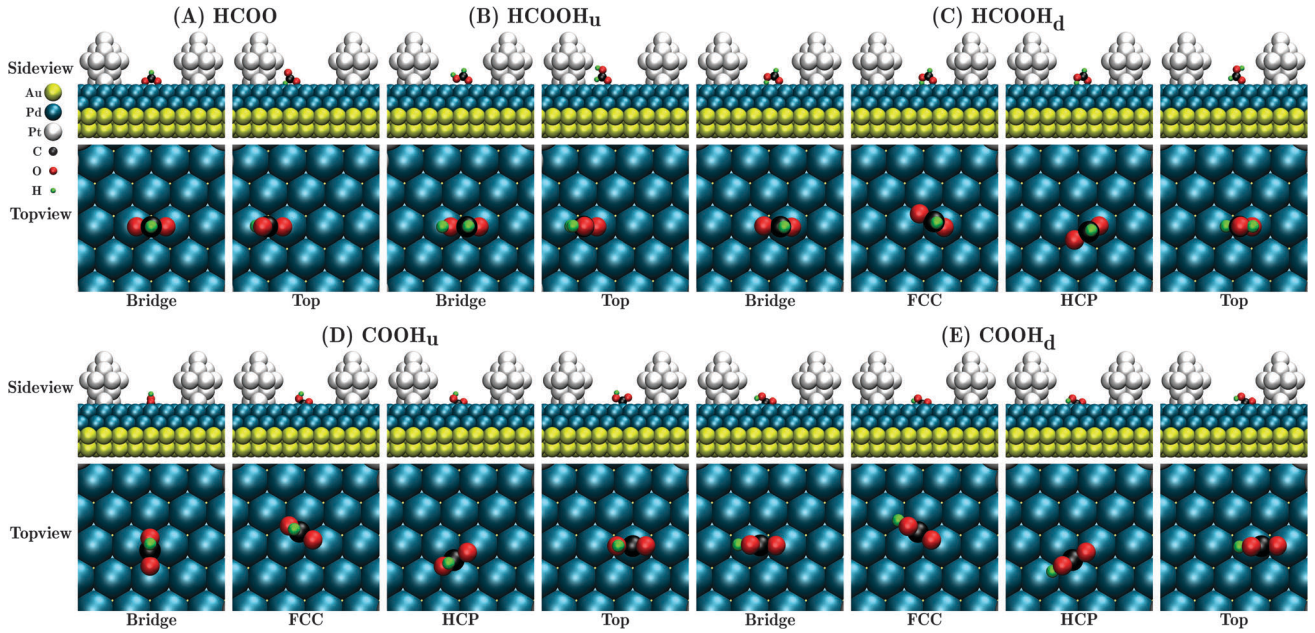

Fig. 3 Optimized structures of (A) HCOO, (B) $HCOOH_u$, (C) $HCOOH_d$, (D) $COOH_u$, and (E) $COOH_d$ adsorbed on different sites in the center area of Au@2 ML Pd@0.5 ML Pt NPs.

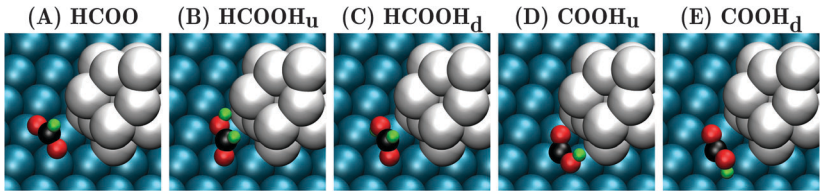

Fig. 4 Tilt view for the optimized structures of (A) HCOO, (B) $HCOOH_u$, (C) $HCOOH_d$, (D) $COOH_u$, and (E) $COOH_d$ adsorbed as close as possible to the Pt cluster in the edge area of Au@2 ML Pd@0.5 ML Pt NPs.

the center area. When the adsorbates are closer to the Pt cluster, they are either adsorbed on the Pt clusters or further decomposed (see Fig. S3–S6 in ESI† for details). Moreover, we found that the dihedral angle of C–O–O–H in the $COOH_u$ is 8°. The distorted structures make further decomposition much easier, which indicates that such an edge area may be a catalytic active site. According to this result and the repulsion between the edge area and the poison intermediate CO, the high electrocatalytic activity of tri-metallic Au@Pd@Pt NPs may be caused by the unique edge area which contains the synergistic effect of the Au core, the Pd shell surface and the mushroom-like Pt cluster.

3.4 Decomposition of COOH

To investigate the effects of the mushroom-like structure for the formic acid oxidation, the decomposition of COOH is considered in this section. COOH has been assumed as an important intermediate in the DFAFCs.[68–71] From the theoretical point of view, COOH is a good substance to study the effects for the indirect/direct pathway since it can be decomposed both through the CO pathway (reaction e) and the CO_2 pathway (reaction f). For the geometric reason, we only considered the $COOH_u$ decomposed through the CO pathway and $COOH_d$ through the CO_2 pathway in the edge and center areas.

The calculated potential energy surfaces (PESs) as well as the optimized structures of stationary points for the CO and CO_2 pathways are depicted in Fig. 5. In the center area, the most stable configurations, *i.e.* adsorbed on the fcc site, were considered as the initial structures. The transition states are similar in different areas for both pathways. For instance, for the CO_2 pathway, the O–H bond is broken in the transition state and the final products are a H atom adsorbed on the

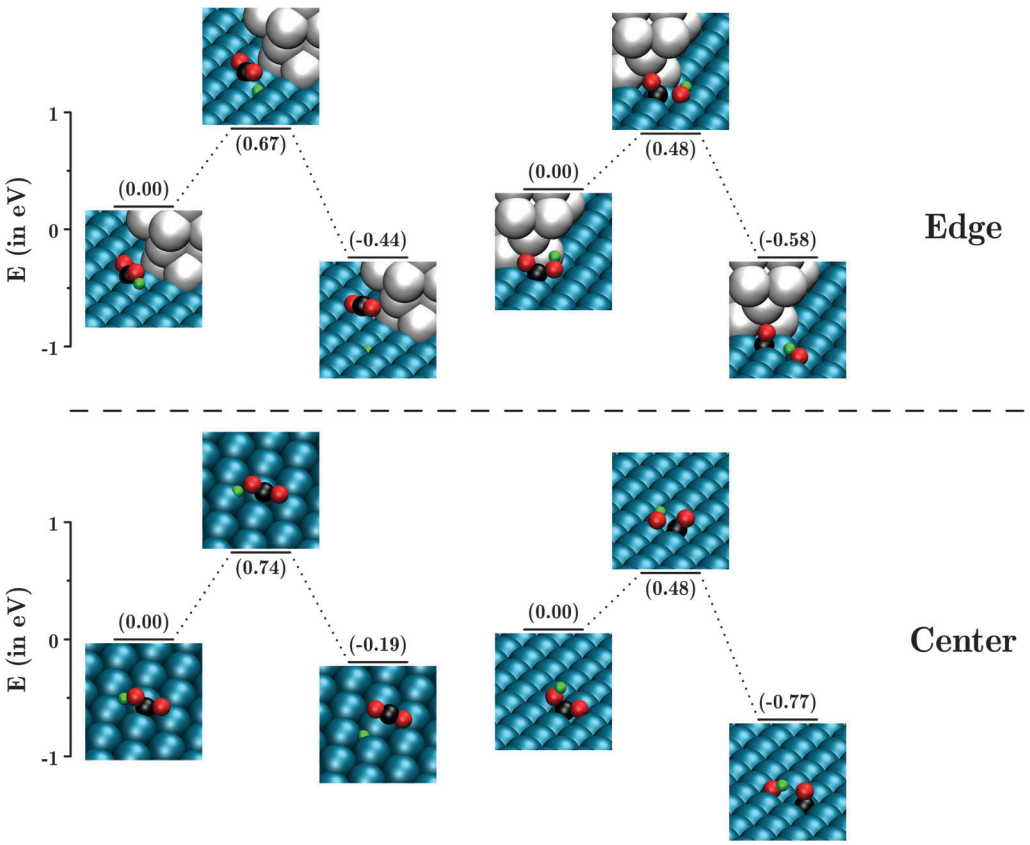

Fig. 5 Potential energy surfaces for the CO_2 pathway (left) and CO pathway (right) in the edge and center areas with the energy of $COOH_d$ adsorbed on the center area as the reference energy. The values in parentheses are the relative energies with respect to the corresponding reactant.

hollow sites and an unbound CO_2. Meanwhile, for the CO pathway, accompanying with the C–O bond breaking, a rotation of H–O–C–O dihedral takes place at the transition state. Finally, the CO pathway produces CO vertically adsorbed on the fcc site and OH adsorbed on the bridge site with a tilted configuration as shown in Fig. 5.

Compared to the center area, the calculated results show that the reaction barrier of the CO_2 pathway in the edge area decreases from 0.74 to 0.67 eV and the released heat increases from 0.19 to 0.44 eV. Meanwhile, for the CO pathway, the reaction barriers in both areas are all around 0.48 eV. Moreover, the released heat of the CO pathway in the edge area is lower than that in the center area (0.58 *vs.* 0.77 eV). These results demonstrate that the CO_2 pathway will be promoted and the CO pathway will be suppressed in the edge area. Thus, the increased probability of the CO_2 pathway should be responsible for the high electrocatalytic activity of Au@Pd@Pt NPs toward formic acid oxidation. Yet, we are not able to rule out the probability of the CO pathway for formic acid oxidation in Au@Pd@Pt systems. In fact, the reaction barrier and released heat indicate that the CO pathway easily occurs in the center area. Moreover, the probability of the CO pathway is comparable with that of the CO_2 pathway even in the edge area (see absolute energies of the transition state in Fig. 5). This result agrees with the *in situ* SERS spectra which showed that the CO molecules are adsorbed on the hollow sites during the oxidation of formic acid.[9]

It is noteworthy that there are other intermediates for the formic acid oxidation.[21,24,72] For instance, Pronkin *et al.*[72] concluded that the HCOO is an intermediate on Pd/Au electrodes for formic acid oxidations as on Pt[73] by using surface-enhanced infrared absorption spectroscopy in the attenuated total reflection mode. However, oxidation of HCOO has really a high active barrier because of the geometric reason as shown on the Pt surface.[74] Moreover, for other adsorbates, the CO_2 pathway should take place more easily with the help of the Pt cluster in the edge area due to the optimized geometries. For instance, the difference in the adsorption energies of the bidentate and monodentate HCOO is reduced from 0.73 eV (in the center area) to 0.23 eV (in the edge area). Apparently, the CO_2 pathway is promoted for the monodentate HCOO because the H is closer to the metallic catalyst. It should be noted that the electrode potential calculated here is near the potential of zero charge, *i.e.* $\sim$0.1 V *vs.* SCE,[75] which is in the startup region of the HCOOH oxidation.[9,34] In this region of potential, the surface concentrations of intermediates should be very low, which is consistent with our simulations. Overall, we can conclude that the CO_2 pathway is considerably promoted in the edge area. Therefore, the simple model employed here without considering solvent effects[22] and electrode potential[76] can still provide useful understanding for formic acid oxidation in Au@Pd@Pt NP systems.

4 Conclusions

In this study, we have investigated the adsorption and decomposition of formic acid on the Au-core@2 ML Pd-shell@0.5 ML Pt-cluster NPs which display high electrocatalytic activity by DFT calculations. The center and edge areas with four typical adsorption sites, bridge, fcc, hcp, and top, are considered in our simulations for adsorption. The calculated results in the center area are consistent with previous studies. On the other hand, our calculations show that the poison intermediate CO of DFAFCs is repulsed significantly in the edge area. Our calculated PESs demonstrate that the CO_2 pathway in the edge area is enhanced compared to that at active sites in the center area. This is probably the origin for the high electrocatalytic activity of Au@Pd@Pt NPs toward the formic acid oxidation. To conclude, the unique mushroom-like structure of Au@Pd@Pt NPs should be the reason for its high electrocatalytic activity for DFAFCs. Such a finding is expected to be helpful for the design of new electrochemical catalysts.

Acknowledgements

This work is supported by the National Natural Science Foundation of China (Grant No. 20620130427, 20925311), the National Basic Research Program of China (Grant No. 2009CB930703, 2010CB923300), Göran Gustafsson Foundation for Research in Natural Sciences and Medicine and the Swedish National Infrastructure for Computing (SNIC).

References

1 N. Tian, Z. Y. Zhou, S. G. Sun, Y. Ding and Z. L. Wang, *Science*, 2007, **316**, 732–735.
2 K. M. Bratlie, H. Lee, K. Komvopoulos, P. Yang and G. A. Somorjai, *Nano Lett.*, 2007, **7**, 3097–3101.
3 Y. Xia, Y. Xiong, B. Lim and S. Skrabalak, *Angew. Chem., Int. Ed.*, 2008, **48**, 60–103.
4 J. Solla-Gullón, F. J. Vidal-Iglesias, A. López-Cudero, E. Garnier, J. M. Feliu and A. Aldaz, *Phys. Chem. Chem. Phys.*, 2008, **10**, 3689–3698.
5 D. Strmcnik, M. Escudero-Escribano, K. Kodama, V. R. Stamenkovic, A. Cuesta and N. M. Marković, *Nat. Chem.*, 2010, **2**, 880–885.
6 I. Hatay, B. Su, M. A. Méndez, C. Corminboeuf, T. Khoury, C. P. Gros, M. Bourdillon, M. Meyer, J. M. Barbe, M. Ersoz, S. Záliš, Z. Samec and H. H. Girault, *J. Am. Chem. Soc.*, 2010, **132**, 13733–13741.
7 H. Lee, S. E. Habas, G. A. Somorjai and P. Yang, *J. Am. Chem. Soc.*, 2008, **130**, 5406–5407.
8 F. J. Vidal-Iglesias, J. Solla-Gullón, E. Herrero, A. Aldaz and J. M. Feliu, *Angew. Chem., Int. Ed.*, 2010, **49**, 6998–7001.
9 P. P. Fang, S. Duan, X. D. Lin, J. R. Anema, J. F. Li, O. Buriez, Y. Ding, F. R. Fan, D. Y. Wu, B. Ren, Z. L. Wang, C. Amatoreb and Z. Q. Tian, *Chem. Sci.*, 2011, **2**, 531–539.
10 F. R. Fan, D. Y. Liu, Y. F. Wu, S. Duan, Z. X. Xie, Z. Y. Jiang and Z. Q. Tian, *J. Am. Chem. Soc.*, 2008, **130**, 6949–6951.
11 W. Schärtl, *Nanoscale*, 2010, **2**, 829–834.
12 B. Lim, J. Wang, P. H. C. Camargo, M. Jiang, M. J. Kim and Y. Xia, *Nano Lett.*, 2008, **8**, 2535–2540.

13 L. Wang and Y. Yamauchi, *J. Am. Chem. Soc.*, 2010, **132**, 13636–13638.
14 Z. Bai, L. Yang, L. Li, J. Lv, K. Wang and J. Zhang, *J. Phys. Chem. C*, 2009, **113**, 10568–10573.
15 Y. W. Rhee, S. Y. Ha and R. I. Masel, *J. Power Sources*, 2003, **117**, 35–38.
16 X. Yu and P. G. Pickup, *J. Power Sources*, 2008, **182**, 124–132.
17 M. Ojeda and E. Iglesia, *Angew. Chem., Int. Ed.*, 2009, **48**, 4800–4803.
18 C. M. Miesse, W. S. Jung, K. J. Jeong, J. K. Lee, J. Lee, J. Han, S. P. Yoon, S. W. Nam, T. H. Lim and S. A. Hong, *J. Power Sources*, 2006, **162**, 532–540.
19 V. Grozovski, V. Climent, E. Herrero and J. M. Feliu, *Phys. Chem. Chem. Phys.*, 2010, **12**, 8822–8831.
20 T. Okada and M. Kaneko, *Molecular Catalysts for Energy Conversion*, Springer, 2008.
21 Y. X. Chen, M. Heinen, Z. Jusys and R. J. Behm, *Angew. Chem., Int. Ed.*, 2006, **45**, 981–985.
22 W. Gao, J. A. Keith, J. Anton and T. Jacob, *J. Am. Chem. Soc.*, 2010, **132**, 18377–18385.
23 R. Larsen, S. Ha, J. Zakzeski and R. I. Masel, *J. Power Sources*, 2006, **157**, 78–84.
24 H. Miyake, T. Okada, G. Samjeské and M. Osawa, *Phys. Chem. Chem. Phys.*, 2008, **10**, 3662–3669.
25 K. Tedsree, T. Li, S. Jones, C. W. A. Chan, K. M. K. Yu, P. A. J. Bagot, E. A. Marquis, G. D. W. Smith and S. C. E. Tsang, *Nat. Nanotechnol.*, 2011, **6**, 302–307.
26 H. X. Zhang, C. Wang, J. Y. Wang, J. J. Zhai and W. B. Cai, *J. Phys. Chem. C*, 2010, **114**, 6446–6451.
27 Q. Yuan, Z. Zhou, J. Zhuang and X. Wang, *Chem. Commun.*, 2010, **46**, 1491–1493.
28 C. Rice, S. Ha, R. I. Masela and A. Wieckowski, *J. Power Sources*, 2003, **115**, 229–235.
29 B. Liu, H. Y. Li, L. Die, X. H. Zhang, Z. Fan and J. H. Chen, *J. Power Sources*, 2009, **186**, 62–66.
30 X. Ji, K. T. Lee, R. Holden, L. Zhang, J. Zhang, G. A. Botton, M. Couillard and L. F. Nazar, *Nat. Chem.*, 2010, **2**, 286–293.
31 B. Blizanac, P. N. Ross and N. M. Markovic, *Electrochim. Acta*, 2007, **52**, 2264–2271.
32 R. Bashyam and P. Zelenay, *Nature*, 2006, **443**, 63–66.
33 S. Uhm, H. J. Lee and J. Lee, *Phys. Chem. Chem. Phys.*, 2009, **11**, 9326–9336.
34 S. Duan, P. P. Fang, F. R. Fan, I. Broadwell, F. Z. Yang, D. Y. Wu, B. Ren, C. Amatore, Y. Luo, X. Xu and Z. Q. Tian, *Phys. Chem. Chem. Phys.*, 2011, **13**, 5441–5449.
35 G. Kresse and J. Furthmüller, *Phys. Rev. B: Condens. Matter Mater. Phys.*, 1996, **54**, 11169–11186.
36 J. P. Perdew, K. Burke and M. Ernzerhof, *Phys. Rev. Lett.*, 1996, **77**, 3865–3868.
37 P. E. Blöchl, O. Jepsen and O. K. Andersen, *Phys. Rev. B: Condens. Matter Mater. Phys.*, 1994, **49**, 16223–16233.
38 G. Kresse and D. Joubert, *Phys. Rev. B: Condens. Matter Mater. Phys.*, 1999, **59**, 1758–1775.
39 H. J. Monkhorst and J. D. Pack, *Phys. Rev. B: Solid State*, 1976, **13**, 5188–5192.
40 N. İnoğlu and J. R. Kitchin, *J. Catal.*, 2009, **261**, 188–194.
41 C. M. Y. Yue and K. H. Lim, *Catal. Lett.*, 2009, **128**, 221–226.
42 *CRC Handbook of Chemistry and Physics*, ed. D. R. Lide, Taylor and Francis, Boca Raton, FL, 87th edn 2007.
43 J. Neugebauer and M. Scheffler, *Phys. Rev. B: Condens. Matter Mater. Phys.*, 1992, **46**, 16067–16080.
44 G. Makov and M. C. Payne, *Phys. Rev. B: Condens. Matter Mater. Phys.*, 1995, **51**, 4014–4022.
45 G. Henkelman, B. P. Uberuaga and H. Jónsson, *J. Chem. Phys.*, 2000, **113**, 9901–9904.
46 G. Henkelman and H. Jónsson, *J. Chem. Phys.*, 2000, **113**, 9978–9985.
47 G. Henkelman and H. Jónsson, *J. Chem. Phys.*, 1999, **111**, 7010–7022.
48 K. Huber and G. Herzberg, *Molecular Spectra and Molecular Structure. IV. Constants of Diatomic Molecules*, Van Nostrand, 1st edn 1979.
49 O. R. Gilliam, C. M. Johnson and W. Gordy, *Phys. Rev.*, 1950, **78**, 140–144.
50 A. Almenningen, O. Bastiansen and T. Motzfeldt, *Acta Chem. Scand.*, 1969, **23**, 2848–2864.
51 W. H. Hocking, *Z. Naturforsch., A: Phys., Phys. Chem., Kosmophys.*, 1976, **31**, 1113–1121.
52 J. R. B. Gomes and J. A. N. F. Gomes, *Surf. Sci.*, 1999, **432**, 279–290.
53 H. T. Chen, J. G. Chang and H. L. Chen, *J. Phys. Chem. A*, 2008, **112**, 8093–8099.
54 G. Buemi, *J. Phys. Org. Chem.*, 2009, **22**, 933–947.
55 A. R. Striganov and N. S. Sventitskii, *Tables of spectral lines of neutral and ionized atoms*, Plenum Press, New York, 1968.
56 Z. Zhouo, Y. Shia, H. Zhanga, X. Zhoua and H. Fu, *THEOCHEM*, 2004, **682**, 1–7.
57 O. Takahashi, K. Itoh, A. Kawano and K. Saito, *THEOCHEM*, 2001, **545**, 197–205.
58 S. R. Langford, A. D. Batten, M. Kono and M. N. R. Ashfold, *J. Chem. Soc., Faraday Trans.*, 1997, **93**, 3757–3764.
59 X. Q. Qi, Z. D. Wei, L. Li, M. B. Ji, L. L. Li, Q. Zhang, M. R. Xia, S. G. Chen and L. J. Yang, *Comput. Theor. Chem.*, 2012, **979**, 96–101.
60 M. Todorova, K. Reuter and M. Scheffler, *J. Phys. Chem. B*, 2004, **108**, 14477–14483.
61 A. A. Phatak, W. N. Delgass, F. H. Ribeiro and W. F. Schneider, *J. Phys. Chem. C*, 2009, **113**, 7269–7276.
62 F. M. Hoffmann, *Surf. Sci. Rep.*, 1983, **3**, 107–192.
63 V. V. Kaichev, I. P. Prosvirin, V. I. Bukhtiyarov, H. Unterhalt, G. Rupprechter and H. J. Freund, *J. Phys. Chem. B*, 2003, **107**, 3522–3527.
64 S. Zou and M. J. Weaver, *J. Phys. Chem.*, 1996, **100**, 4237–4242.
65 K. Honkala, P. Pirilä and K. Laasonen, *Phys. Rev. Lett.*, 2001, **25**, 5942–5945.
66 T. Zheng, D. Stacchiola, D. K. Saldin, J. James, D. S. Sholl and W. T. Tysoe, *Surf. Sci.*, 2005, **574**, 166–174.
67 J. Y. Wang, H. X. Zhang, K. Jiang and W. B. Cai, *J. Am. Chem. Soc.*, 2011, **113**, 14876–14879.
68 A. Capon and R. Parson, *J. Electroanal. Chem.*, 1973, **44**, 1–7.
69 A. Capon and R. Parson, *J. Electroanal. Chem.*, 1974, **44**, 239–254.

70 A. Capon and R. Parsons, *J. Electroanal. Chem.*, 1973, **45**, 205–231.
71 R. R. Adić, M. D. Spasojević and A. R. Despić, *J. Electroanal. Chem.*, 1978, **92**, 31–43.
72 S. Pronkin, M. Hara and T. Wandlowski, *Russ. J. Electrochem.*, 2006, **42**, 1177–1192.
73 A. Miki, S. Ye and M. Osawa, *Chem. Commun.*, 2002, 1500–1501.
74 H. F. Wang and Z. P. Liu, *J. Phys. Chem. C*, 2009, **113**, 17502–17508.
75 A. El-Aziz, L. Kibler and D. Kolb, *Electrochem. Commun.*, 2002, **4**, 535–539.
76 J. K. Nørskov, J. Rossmeisl, A. Logadottir, L. Lindqvist, J. R. Kitchin, T. Bligaard and H. Jónsson, *J. Phys. Chem. B*, 2004, **108**, 17886–17892.